
12.1. Introduction

Modern airborne radar systems are designed to perform a large number of functions which range from detection and discrimination of targets to mapping large areas of ground terrain. This mapping can be performed by the Synthetic Aperture Radar (SAR). Through illuminating the ground with coherent radiation and measuring the echo signals, SAR can produce high resolution two-dimensional (and in some cases three-dimensional) imagery of the ground surface. The quality of ground maps generated by SAR is determined by the size of the resolution cell. A resolution cell is specified by range and azimuth resolutions of the system. Other factors affecting the size of the resolution cells are (1) size of the processed map and the amount of signal processing involved; (2) cost consideration; and (3) size of the objects that need to be resolved in the map. For example, mapping gross features of cities and coastlines does not require as much resolution when compared to resolving houses, vehicles, and streets.

SAR systems can produce maps of reflectivity versus range and Doppler (cross range). Range resolution is accomplished through range gating. Fine range resolution can be accomplished by using pulse compression techniques. The azimuth resolution depends on antenna size and radar wavelength. Fine azimuth resolution is enhanced by taking advantage of the radar motion in order to synthesize a larger antenna aperture. Let N_r denote the number of range bins and let N_a denote the number of azimuth cells. It follows that the total number of resolution cells in the map is $N_r N_a$. SAR systems that are

generally concerned with improving azimuth resolution are often referred to as Doppler Beam-Sharpening (DBS) SARs. In this case, each range bin is processed to resolve targets in Doppler which correspond to azimuth. This chapter is presented in the context of DBS.

Due to the large amount of signal processing required in SAR imagery, the early SAR designs implemented optical processing techniques. Although such optical processors can produce high quality radar images, they have several shortcomings. They can be very costly and are, in general, limited to making strip maps. Motion compensation is not easy to implement for radars that utilize optical processors. With the recent advances in solid state electronics and Very Large Scale Integration (VLSI) technologies, digital signal processing in real time has been made possible in SAR systems.

12.2. Real Versus Synthetic Arrays

A linear array of size N , element spacing d , isotropic elements, and wavelength λ is shown in Fig. 12.1. A synthetic linear array is formed by linear motion of a single element, transmitting and receiving from distinct positions that correspond to the element locations in a real array. Thus, synthetic array geometry is similar to that of a real array, with the exception that the array exists only at a single element position at a time.

The two-way radiation pattern (in the direction-sine $\sin\beta$) for a real linear array was developed in Chapter 10; it is repeated here as Eq. (12.1):

$$G(\sin\beta) = \left(\frac{\sin((Nkd\sin\beta)/2)}{\sin((kd\sin\beta)/2)} \right)^2 \quad (12.1)$$

Since a synthetic array exists only at a single location at a time, the array transmission is sequential with only one element receiving. Therefore, the returns received by the successive array positions differ in phase by $\delta = k\Delta r$, where $k = 2\pi/\lambda$, and $\Delta r = 2d\sin\beta$ is the round-trip path difference between contiguous element positions. The two-way array pattern for a synthetic array is the coherent sum of the returns at all the array positions.

Thus, the overall two-way electric field for the synthetic array is

$$E(\sin\beta) = 1 + e^{-j2\delta} + e^{-j4\delta} + \dots + e^{-j2(N-1)\delta} = \sum_{n=1}^N e^{-j2(N-1)kd\sin\beta} \quad (12.2)$$

By using similar analysis as in Section 10.4, the two-way electric field for a synthetic array can be expressed as

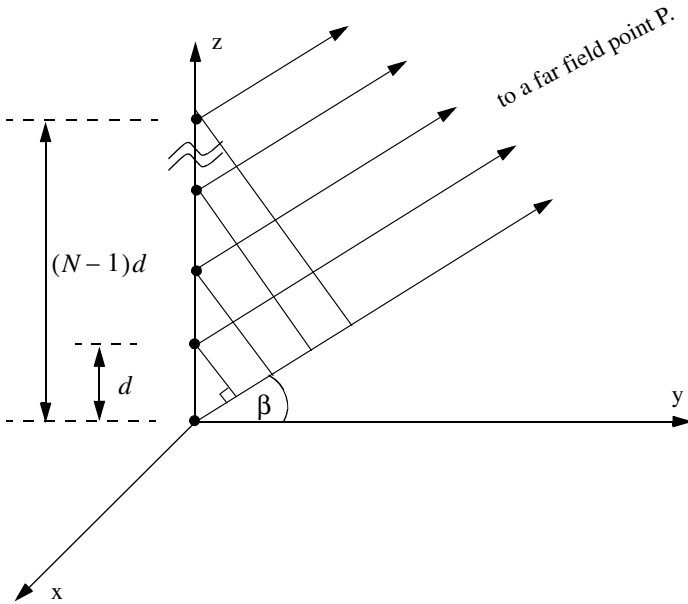


Figure 12.1. Geometry of real or synthetic array.

$$E(\sin \beta) = \frac{\sin(Nkd \sin \beta)}{\sin(kd \sin \beta)} \quad (12.3)$$

and the two-way radiation pattern is

$$G(\sin \beta) = |E(\sin \beta)| = \left| \frac{\sin(Nkd \sin \beta)}{\sin(kd \sin \beta)} \right| \quad (12.4)$$

Comparison of Eq. (12.4) and Eq. (12.1) indicates that the two-way radiation pattern for a real array is of the form $(\sin \theta / \theta)^2$, while it is of the form $\sin 2\theta / 2\theta$ for the synthetic array. Consequently, for the same size aperture, the main beam of the synthetic array is twice as narrow as that for the real array. Or equivalently, the resolution of a synthetic array of length L (aperture size) is equal to that of a real array with twice the aperture size ($2L$), as illustrated in Fig. 12.2.

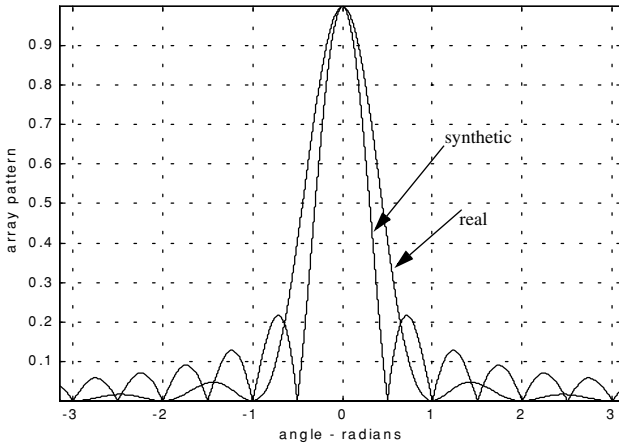


Figure 12.2. Pattern difference between real and synthetic arrays. This plot can be reproduced using MATLAB program “fig12_2.m” given in Listing 12.1 in Section 12.12.

12.3. Side Looking SAR Geometry

Fig. 12.3 shows the geometry for the standard side looking SAR. We will assume that the platform carrying the radar maintains both fixed altitude h and velocity v . The antenna $3dB$ beam width is θ , and the elevation angle (measured from the z -axis to the antenna axis) is β . The intersection of the antenna beam with the ground defines a footprint. As the platform moves, the footprint scans a swath on the ground.

The radar position with respect to the absolute origin $\vec{O} = (0, 0, 0)$, at any time is the vector $\vec{a}(t)$. The velocity vector $\vec{a}'(t)$ is

$$\vec{a}'(t) = 0 \times \hat{a}_x + v \times \hat{a}_y + 0 \times \hat{a}_z \quad (12.5)$$

The Line of Sight (LOS) for the current footprint centered at $\vec{q}(t_c)$ is defined by the vector $\vec{R}(t_c)$, where t_c denotes the central time of the observation interval T_{ob} (coherent integration interval). More precisely,

$$(t = t_a + t_c) ; -\frac{T_{ob}}{2} \leq t \leq \frac{T_{ob}}{2} \quad (12.6)$$

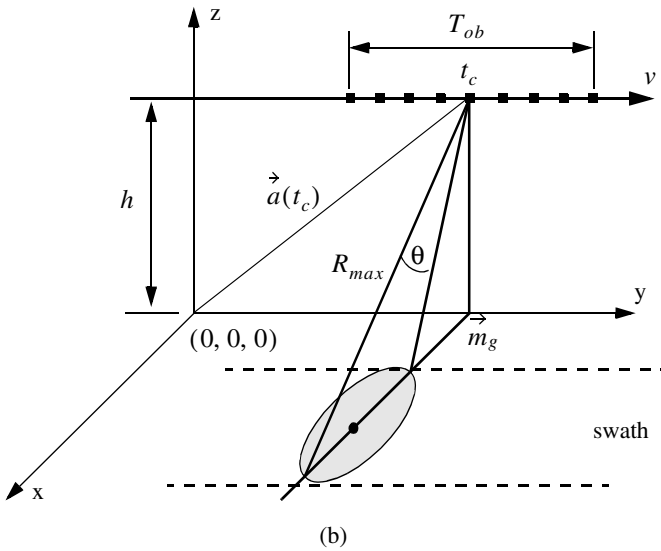
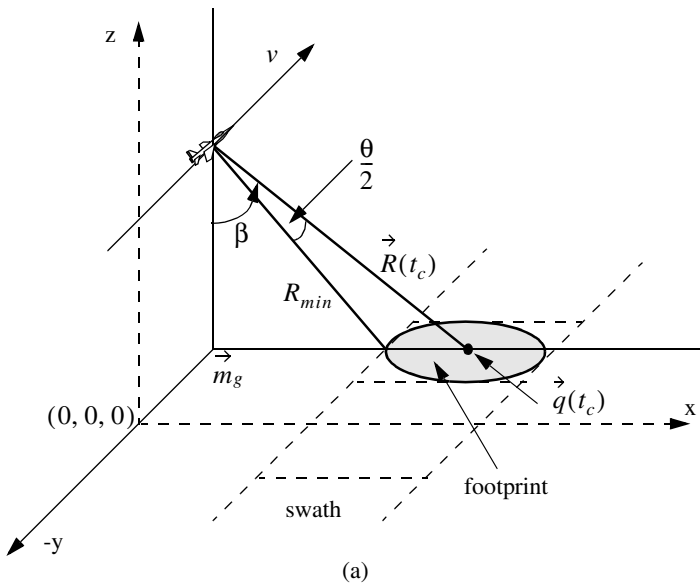


Figure 12.3. Side looking SAR geometry.

where t_a and t are the absolute and relative times, respectively. The vector \vec{m}_g defines the ground projection of the antenna at central time. The minimum slant range to the swath is R_{min} , and the maximum range is denoted R_{max} , as illustrated by Fig. 12.4. It follows that

$$\begin{aligned} R_{min} &= h / \cos(\beta - \theta/2) \\ R_{max} &= h / \cos(\beta + \theta/2) \\ \left| \vec{R}(t_c) \right| &= h / \cos \beta \end{aligned} \tag{12.7}$$

Notice that the elevation angle β is equal to

$$\beta = 90 - \psi_g \tag{12.8}$$

where ψ_g is the grazing angle. The size of the footprint is a function of the grazing angle and the antenna beam width, as illustrated in Fig. 12.5. The SAR geometry described in this section is referred to as SAR “strip mode” of operation. Another SAR mode of operation, which will not be discussed in this chapter, is called “spot-light mode,” where the antenna is steered (mechanically or electronically) to continuously illuminate one spot (footprint) on the ground. In this case, one high resolution image of the current footprint is generated during an observation interval.

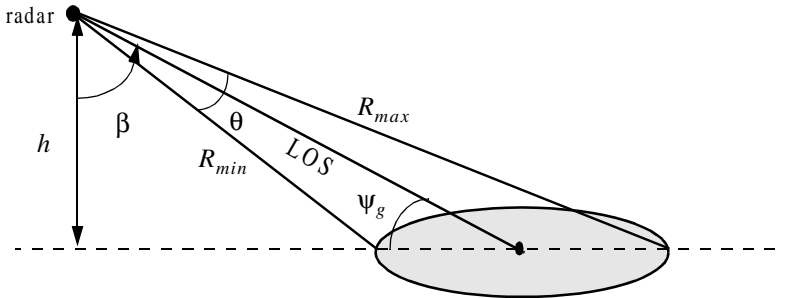


Figure 12.4. Definition of minimum and maximum range.

12.4. SAR Design Considerations

The quality of SAR images is heavily dependent on the size of the map resolution cell shown in Fig. 12.6. The range resolution, ΔR , is computed on the beam LOS, and is given by

$$\Delta R = (c\tau)/2 \tag{12.9}$$

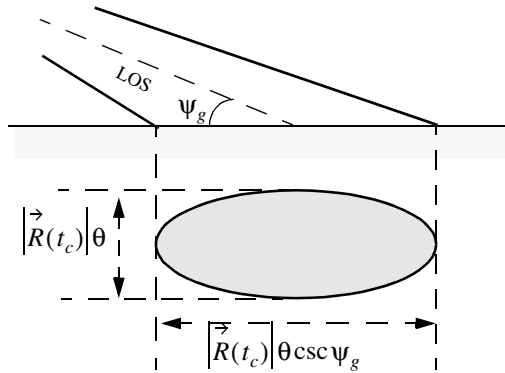


Figure 12.5. Footprint definition.

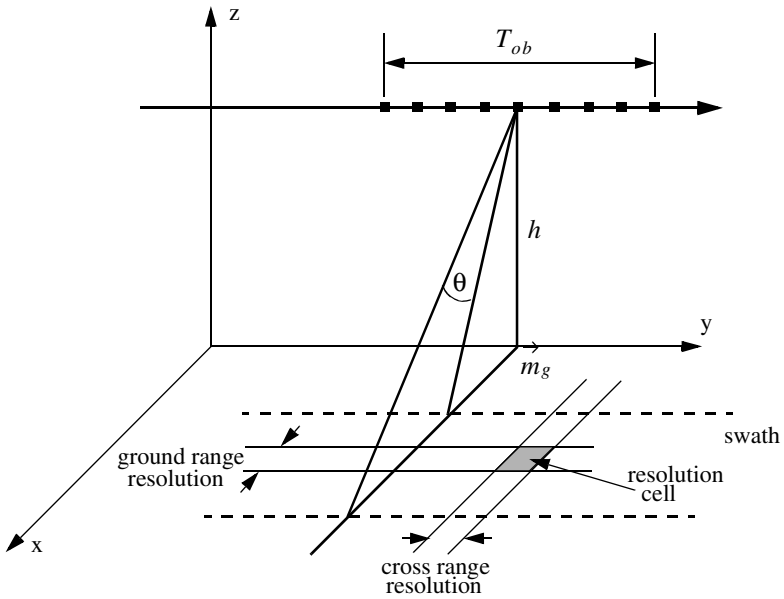


Figure 12.6. Definition of a resolution cell.

where τ is the pulse width. From the geometry in Fig. 12.7 the extent of the range cell ground projection ΔR_g is computed as

$$\Delta R_g = \frac{c\tau}{2} \sec \psi_g \quad (12.10)$$

The azimuth or cross range resolution for a real antenna with a $3dB$ beam width θ (radians) at range R is

$$\Delta A_r = \theta R \quad (12.11)$$

However, the antenna beam width is proportional to the aperture size,

$$\theta \approx \frac{\lambda}{L} \quad (12.12)$$

where λ is the wavelength and L is the aperture length. It follows that

$$\Delta A_r = \frac{\lambda R}{L} \quad (12.13)$$

And since the effective synthetic aperture size is twice that of a real array, the azimuth resolution for a synthetic array is then given by

$$\Delta A = \frac{\lambda R}{2L} \quad (12.14)$$

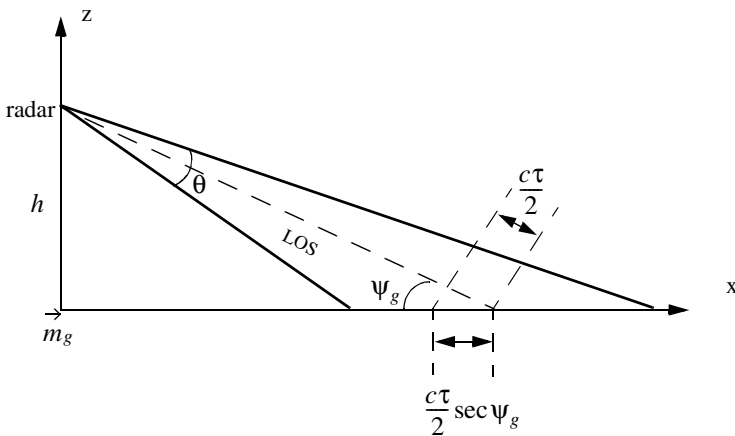


Figure 12.7. Definition of a range cell on the ground.

Furthermore, since the synthetic aperture length L is equal to vT_{ob} , Eq. (12.14) can be rewritten as

$$\Delta A = \frac{\lambda R}{2vT_{ob}} \quad (12.15)$$

The azimuth resolution can be greatly improved by taking advantage of the Doppler variation within a footprint (or a beam). As the radar travels along its flight path the radial velocity to a ground scatterer (point target) within a footprint varies as a function of the radar radial velocity in the direction of that scatterer. The variation of Doppler frequency for a certain scatterer is called the ‘‘Doppler history.’’

Let $R(t)$ denote range to a scatterer at time t , and v_r be the corresponding radial velocity; thus the Doppler shift is

$$f_d = - \frac{2R'(t)}{\lambda} = \frac{2v_r}{\lambda} \quad (12.16)$$

where $R'(t)$ is the range rate to the scatterer. Let t_1 and t_2 be the times when the scatterer enters and leaves the radar beam, respectively, and let t_c be the time that corresponds to minimum range. Fig. 12.8 shows a sketch of the corresponding $R(t)$ (see Eq. (12.16)). Since the radial velocity can be computed as the derivative of $R(t)$ with respect to time, one can clearly see that Doppler frequency is maximum at t_1 , zero at t_c , and minimum at t_2 , as illustrated in Fig. 12.9.

In general, the radar maximum PRF, $f_{r_{max}}$, must be low enough to avoid range ambiguity. Alternatively, the minimum PRF, $f_{r_{min}}$, must be high enough to avoid Doppler ambiguity. SAR unambiguous range must be at least as wide as the extent of a footprint. More precisely, since target returns from maximum range due to the current pulse must be received by the radar before the next pulse is transmitted, it follows that SAR unambiguous range is given by

$$R_u = R_{max} - R_{min} \quad (12.17)$$

An expression for unambiguous range was derived in Chapter 1, and is repeated here as Eq. (12.18),

$$R_u = \frac{c}{2f_r} \quad (12.18)$$

Combining Eq. (12.18) and Eq. (12.17) yields

$$f_{r_{max}} \leq \frac{c}{2(R_{max} - R_{min})} \quad (12.19)$$

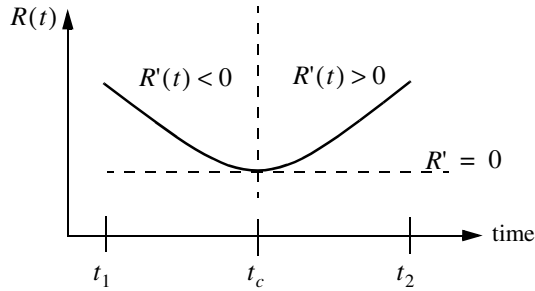


Figure 12.8. Sketch of range versus time for a scatterer.

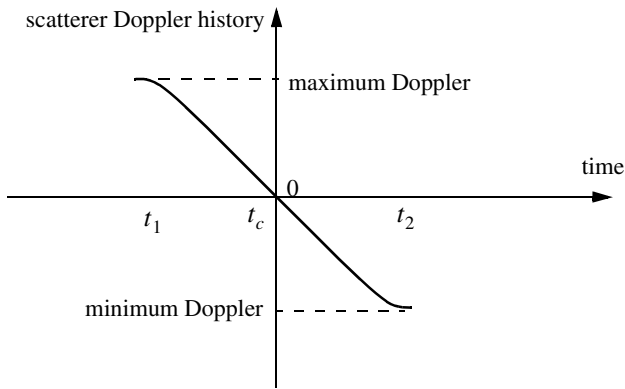
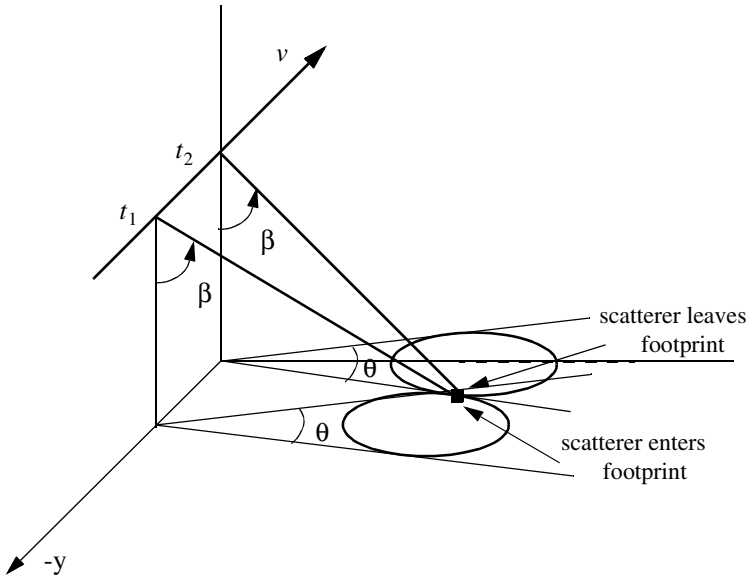


Figure 12.9. Point scatterer Doppler history.

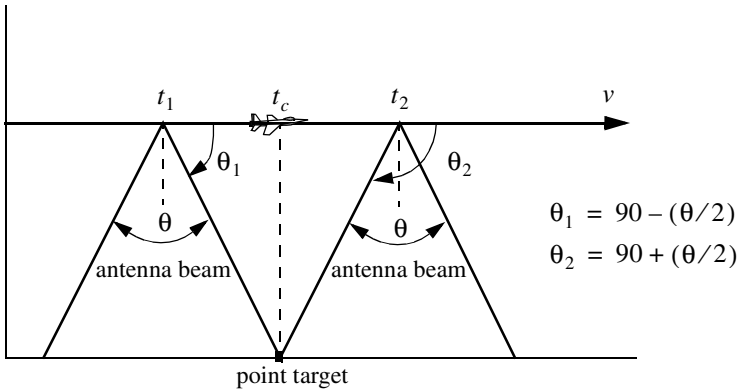
SAR minimum PRF, $f_{r_{min}}$, is selected so that Doppler ambiguity is avoided. In other words, $f_{r_{min}}$ must be greater than the maximum expected Doppler spread within a footprint. From the geometry of Fig. 12.10, the maximum and minimum Doppler frequencies are, respectively, given by

$$\left(f_{d_{max}} = \frac{2v}{\lambda} \cos\left(90 - \frac{\theta}{2}\right) \sin\beta \right) ; \text{ at } t_1 \quad (12.20)$$

$$\left(f_{d_{min}} = \frac{2v}{\lambda} \cos\left(90 + \frac{\theta}{2}\right) \sin\beta \right) ; \text{ at } t_2 \quad (12.21)$$



(a)



(b)

Figure 12.10. Doppler history computation. (a) Full view; (b) top view.

It follows that the maximum Doppler spread is

$$\Delta f_d = f_{d_{max}} - f_{d_{min}} \quad (12.22)$$

Substituting Eqs. (11.20) and (11.21) into Eq. (12.22) and applying the proper trigonometric identities yield

$$\Delta f_d = \frac{4v}{\lambda} \sin \frac{\theta}{2} \sin \beta \quad (12.23)$$

Finally, by using the small angle approximation we get

$$\Delta f_d \approx \frac{4v}{\lambda} \frac{\theta}{2} \sin \beta = \frac{2v}{\lambda} \theta \sin \beta \quad (12.24)$$

Therefore, the minimum PRF is

$$f_{r_{min}} \geq \frac{2v}{\lambda} \theta \sin \beta \quad (12.25)$$

Combining Eqs. (11.19) and (11.25) we get

$$\frac{c}{2(R_{max} - R_{min})} \geq f_r \geq \frac{2v}{\lambda} \theta \sin \beta \quad (12.26)$$

It is possible to resolve adjacent scatterers at the same range within a footprint based only on the difference of their Doppler histories. For this purpose, assume that the two scatterers are within the k th range bin. Denote their angular displacement as $\Delta\theta$, and let $\Delta f_{d_{min}}$ be the minimum Doppler spread between the two scatterers such that they will appear in two distinct Doppler filters. Using the same methodology that led to Eq. (12.24) we get

$$\Delta f_{d_{min}} = \frac{2v}{\lambda} \Delta\theta \sin \beta_k \quad (12.27)$$

where β_k is the elevation angle corresponding to the k th range bin.

The bandwidth of the individual Doppler filters must be equal to the inverse of the coherent integration interval T_{ob} (i.e., $\Delta f_{d_{min}} = 1/T_{ob}$). It follows that

$$\Delta\theta = \frac{\lambda}{2vT_{ob} \sin \beta_k} \quad (12.28)$$

Substituting L for vT_{ob} yields

$$\Delta\theta = \frac{\lambda}{2L\sin\beta_k} \quad (12.29)$$

Therefore, the SAR azimuth resolution (within the k th range bin) is

$$\Delta A_g = \Delta\theta R_k = R_k \frac{\lambda}{2L\sin\beta_k} \quad (12.30)$$

Note that when $\beta_k = 90^\circ$, Eq. (12.30) is identical to Eq. (12.14).

12.5. SAR Radar Equation

The single pulse radar equation was derived in Chapter 1, and is repeated here as Eq. (12.31),

$$SNR = \frac{P_t G^2 \lambda^2 \sigma}{(4\pi)^3 R_k^4 k T_0 B L_{Loss}} \quad (12.31)$$

where: P_t is peak power; G is antenna gain; λ is wavelength; σ is radar cross section; R_k is radar slant range to the k th range bin; k is Boltzman's constant; T_0 is receiver noise temperature; B is receiver bandwidth; and L_{Loss} is radar losses. The radar cross section is a function of the radar resolution cell and terrain reflectivity. More precisely,

$$\sigma = \sigma^0 \Delta R_g \Delta A_g = \sigma^0 \Delta A_g \frac{c\tau}{2} \sec\Psi_g \quad (12.32)$$

where σ^0 is the clutter scattering coefficient, ΔA_g is the azimuth resolution, and Eq. (12.10) was used to replace the ground range resolution. The number of coherently integrated pulses within an observation interval is

$$n = f_r T_{ob} = \frac{f_r L}{v} \quad (12.33)$$

where L is the synthetic aperture size. Using Eq. (12.30) in Eq. (12.33) and rearranging terms yield

$$n = \frac{\lambda R f_r}{2 \Delta A_g v} \csc\beta_k \quad (12.34)$$

The radar average power over the observation interval is

$$P_{av} = (P_t/B) f_r \quad (12.35)$$

The SNR for n coherently integrated pulses is then

$$(SNR)_n = nSNR = n \frac{P_i G^2 \lambda^2 \sigma}{(4\pi)^3 R_k^4 k T_0 B L_{Loss}} \quad (12.36)$$

Substituting Eqs. (11.35), (11.34), and (11.32) into Eq. (12.36) and performing some algebraic manipulations give the SAR radar equation,

$$(SNR)_n = \frac{P_{av} G^2 \lambda^3 \sigma^0}{(4\pi)^3 R_k^3 k T_0 L_{Loss}} \frac{\Delta R_g}{2v} \csc \beta_k \quad (12.37)$$

Eq. (12.37) leads to the conclusion that in SAR systems the SNR is (1) inversely proportional to the third power of range; (2) independent of azimuth resolution; (3) function of the ground range resolution; (4) inversely proportional to the velocity v ; and (5) proportional to the third power of wavelength.

12.6. SAR Signal Processing

There are two signal processing techniques to sequentially produce a SAR map or image; they are line-by-line processing and Doppler processing. The concept of SAR line-by-line processing is as follows. Through the radar linear motion a synthetic array is formed, where the elements of the current synthetic array correspond to the position of the antenna transmissions during the last observation interval. Azimuth resolution is obtained by forming narrow synthetic beams through combination of the last observation interval returns. Fine range resolution is accomplished in real time by utilizing range gating and pulse compression. For each range bin and each of the transmitted pulses during the last observation interval, the returns are recorded in a two-dimensional array of data that is updated for every pulse. Denote the two-dimensional array of data as *MAP*.

To further illustrate the concept of line-by-line processing, consider the case where a map of size $N_a \times N_r$ is to be produced, N_a is the number of azimuth cells, and N_r is the number of range bins. Hence, *MAP* is of size $N_a \times N_r$, where the columns refer to range bins, and the rows refer to azimuth cells. For each transmitted pulse, the echoes from consecutive range bins are recorded sequentially in the first row of *MAP*. Once the first row is completely filled (i.e., returns from all range bins have been received), all data (in all rows) are shifted downward one row before the next pulse is transmitted. Thus, one row of *MAP* is generated for every transmitted pulse. Consequently, for the current observation interval, returns from the first transmitted pulse will be located in the bottom row of *MAP*, and returns from the last transmitted pulse will be in the first row of *MAP*.

In SAR Doppler processing, the array MAP is updated once every N pulses so that a block of N columns is generated simultaneously. In this case, N refers to the number of transmissions during an observation interval (i.e., size of the synthetic array). From an antenna point of view, this is equivalent to having N adjacent synthetic beams formed in parallel through electronic steering.

12.7. Side Looking SAR Doppler Processing

Consider the geometry shown in Fig. 12.11, and assume that the scatterer C_i is located within the k th range bin. The scatterer azimuth and elevation angles are μ_i and β_i , respectively. The scatterer elevation angle β_i is assumed to be equal to β_k , the range bin elevation angle. This assumption is true if the ground range resolution, ΔR_g , is small; otherwise, $\beta_i = \beta_k + \epsilon_i$ for some small ϵ_i ; in this chapter $\epsilon_i = 0$.

The normalized transmitted signal can be represented by

$$s(t) = \cos(2\pi f_0 t - \xi_0) \tag{12.38}$$

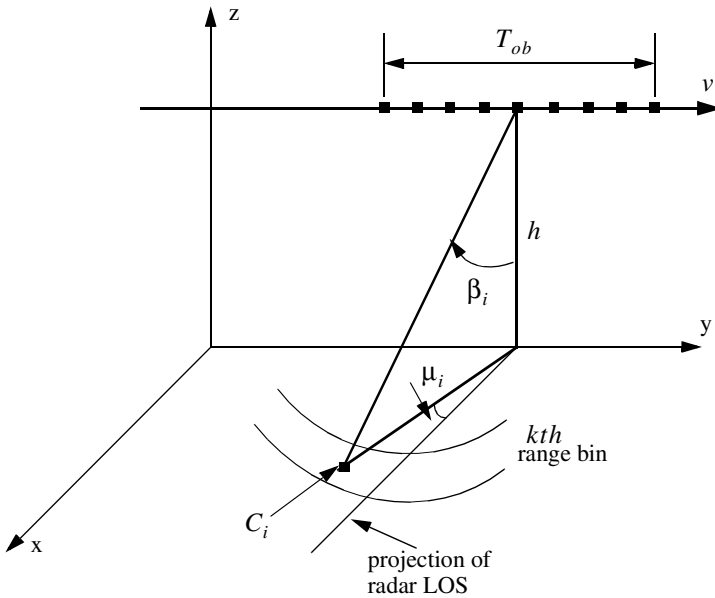


Figure 12.11. A scatterer C_i within the k th range bin.

where f_0 is the radar operating frequency, and ξ_0 denotes the transmitter phase. The returned radar signal from C_i is then equal to

$$s_i(t, \mu_i) = A_i \cos[2\pi f_0(t - \tau_i(t, \mu_i)) - \xi_0] \quad (12.39)$$

where $\tau_i(t, \mu_i)$ is the round-trip delay to the scatterer, and A_i includes scatterer strength, range attenuation, and antenna gain. The round-trip delay is

$$\tau_i(t, \mu_i) = \frac{2r_i(t, \mu_i)}{c} \quad (12.40)$$

where c is the speed of light and $r_i(t, \mu_i)$ is the scatterer slant range. From the geometry in Fig. 12.11, one can write the expression for the slant range to the i th scatterer within the k th range bin as

$$r_i(t, \mu_i) = \frac{h}{\cos \beta_i} \sqrt{1 - \frac{2vt}{h} \cos \beta_i \cos \mu_i \sin \beta_i + \left(\frac{vt}{h} \cos \beta_i\right)^2} \quad (12.41)$$

And by using Eq. (12.40) the round-trip delay can be written as

$$\tau_i(t, \mu_i) = \frac{2}{c} \frac{h}{\cos \beta_i} \sqrt{1 - \frac{2vt}{h} \cos \beta_i \cos \mu_i \sin \beta_i + \left(\frac{vt}{h} \cos \beta_i\right)^2} \quad (12.42)$$

The round-trip delay can be approximated using a two-dimensional second order Taylor series expansion about the reference state $(t, \mu) = (0, 0)$. Performing this Taylor series expansion yields

$$\tau_i(t, \mu_i) \approx \bar{\tau} + \bar{\tau}_{t\mu} \mu_i t + \bar{\tau}_{tt} \frac{t^2}{2} \quad (12.43)$$

where the over-bar indicates evaluation at the state $(0, 0)$, and the subscripts denote partial derivatives. For example, $\tau_{t\mu}$ means

$$\bar{\tau}_{t\mu} = \left. \frac{\partial^2}{\partial t \partial \mu} \tau_i(t, \mu_i) \right|_{(t, \mu) = (0, 0)} \quad (12.44)$$

The Taylor series coefficients are (see Problem 11.6)

$$\bar{\tau} = \left(\frac{2h}{c}\right) \frac{1}{\cos \beta_i} \quad (12.45)$$

$$\bar{\tau}_{t\mu} = \left(\frac{2v}{c}\right) \sin \beta_i \quad (12.46)$$

$$\bar{\tau}_{it} = \left(\frac{2v^2}{hc}\right)\cos\beta_i \quad (12.47)$$

Note that other Taylor series coefficients are either zeros or very small, hence they are neglected. Finally, by substituting Eqs. (12.45) through (12.47) into Eq. (12.43), we can rewrite the returned radar signal as

$$s_i(t, \mu_i) = A_i \cos[\psi_i(t, \mu_i) - \xi_0] \quad (12.48)$$

$$\hat{\psi}_i(t, \mu_i) = 2\pi f_0 \left[(1 - \bar{\tau}_{it}\mu_i)t - \bar{\tau} - \bar{\tau}_{it} \frac{t^2}{2} \right]$$

Observation of Eq. (12.48) indicates that the instantaneous frequency for the *i*th scatterer varies as a linear function of time due to the second order phase term $2\pi f_0(\bar{\tau}_{it}t^2/2)$ (this confirms the result we concluded about a scatterer Doppler history). Furthermore, since this phase term is range-bin dependent and not scatterer dependent, all scatterers within the same range bin produce this exact second order phase term. It follows that scatterers within a range bin have identical Doppler histories. These Doppler histories are separated by the time delay required to fly between them, as illustrated in Fig. 12.12.

Suppose that there are *I* scatterers within the *k*th range bin. In this case, the combined returns for this cell are the sum of the individual returns due to each scatterer as defined by Eq. (12.48). In other words, superposition holds, and the overall echo signal is

$$s_r(t) = \sum_{i=1}^I s_i(t, \mu_i) \quad (12.49)$$

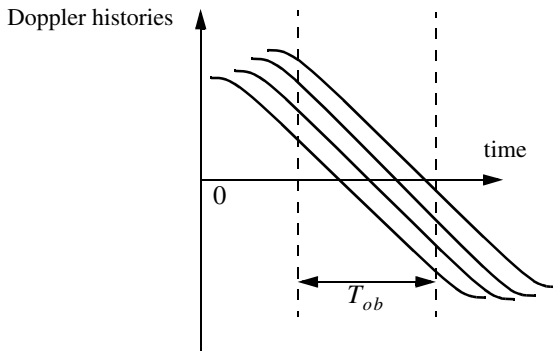


Figure 12.12. Doppler histories for several scatterers within the same range bin.

A signal processing block diagram for the k th range bin is illustrated in Fig. 12.13. It consists of the following steps. First, heterodyning with carrier frequency is performed to extract the quadrature components.

This is followed by LP filtering and A/D conversion. Next, deramping or focusing to remove the second order phase term of the quadrature components is carried out using a phase rotation matrix. The last stage of the processing includes windowing, performing FFT on the windowed quadrature components, and scaling of the amplitude spectrum to account for range attenuation and antenna gain.

The discrete quadrature components are

$$\begin{aligned}\tilde{x}_I(t_n) &= \tilde{x}_I(n) = A_i \cos[\tilde{\Psi}_i(t_n, \mu_i) - \xi_0] \\ \tilde{x}_Q(t_n) &= \tilde{x}_Q(n) = A_i \sin[\tilde{\Psi}_i(t_n, \mu_i) - \xi_0]\end{aligned}\tag{12.50}$$

$$\tilde{\Psi}_i(t_n, \mu_i) = \hat{\Psi}_i(t_n, \mu_i) - 2\pi f_0 t_n\tag{12.51}$$

and t_n denotes the n th sampling time (remember that $-T_{ob}/2 \leq t_n \leq T_{ob}/2$). The quadrature components after deramping (i.e., removal of the phase $\psi = -\pi f_0 \tilde{\tau}_i t_n^2$) are given by

$$\begin{bmatrix} x_I(n) \\ x_Q(n) \end{bmatrix} = \begin{bmatrix} \cos \psi & -\sin \psi \\ \sin \psi & \cos \psi \end{bmatrix} \begin{bmatrix} \tilde{x}_I(n) \\ \tilde{x}_Q(n) \end{bmatrix}\tag{12.52}$$

12.8. SAR Imaging Using Doppler Processing

It was mentioned earlier that SAR imaging is performed using two orthogonal dimensions (range and azimuth). Range resolution is controlled by the receiver bandwidth and pulse compression. Azimuth resolution is limited by the antenna beam width. A one-to-one correspondence between the FFT bins and the azimuth resolution cells can be established by utilizing the signal model described in the previous section. Therefore, the problem of target detection is transformed into a spectral analysis problem, where detection is based on the amplitude spectrum of the returned signal. The FFT frequency resolution Δf is equal to the inverse of the observation interval T_{ob} . It follows that a peak in the amplitude spectrum at $k_1 \Delta f$ indicates the presence of a scatterer at frequency $f_{d1} = k_1 \Delta f$.

For an example, consider the scatterer C_i within the k th range bin. The instantaneous frequency f_{di} corresponding to this scatterer is

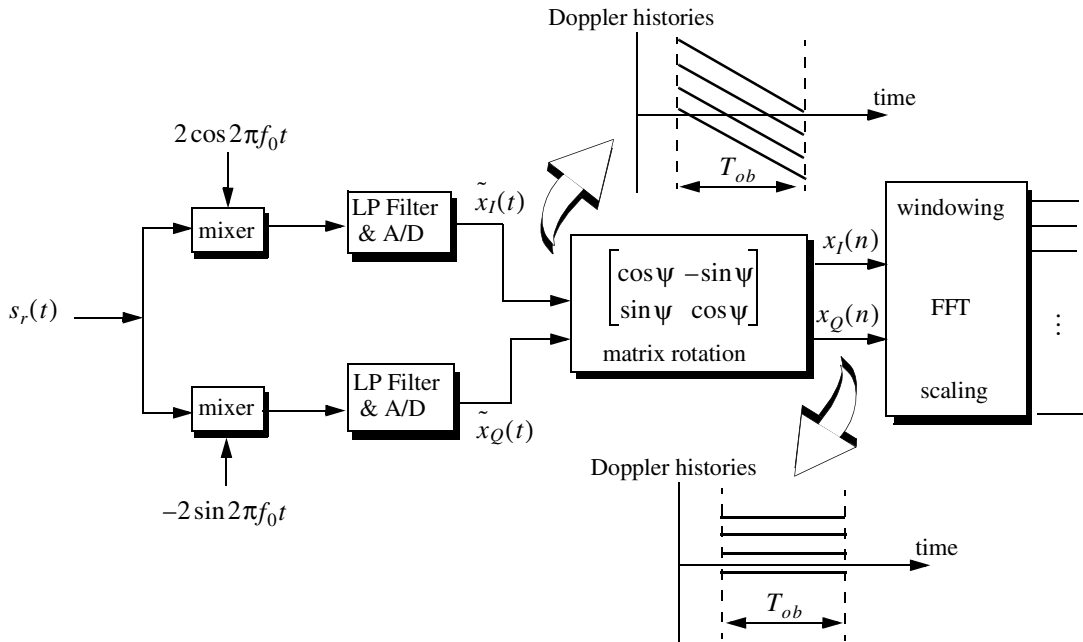


Figure 12.13. Signal processing block diagram for the k th range bin.

$$f_{di} = \frac{1}{2\pi} \frac{d\psi}{dt} = f_0 \bar{\tau}_{r\mu} \mu_i = \frac{2v}{\lambda} \sin\beta_i \mu_i \quad (12.53)$$

which is the same result derived in Eq. (12. 27), where $\mu_i = \Delta\theta$. Therefore, the scatterers separated in Doppler by a frequency greater than Δf can then be resolved.

12.9. Range Walk

As shown earlier SAR Doppler processing is achieved in two steps: first, range gating and second, azimuth compression within each bin at the end of the observation interval. For this purpose, azimuth compression assumes that each scatterer remains within the same range bin during the observation interval. However, since the range gates are defined with respect to a radar that is moving, the range gate grid is also moving relative to the ground. As a result a scatterer appears to be moving within its range bin. This phenomenon is known as range walk. A small amount of range walk does not bother Doppler processing as long as the scatterer remains within the same range bin. However, range walk over several range bins can constitute serious problems, where in this case Doppler processing is meaningless.

12.10. Case Study

Table 12.1 lists the selected design system parameters. The 3 dB element beamwidth is $\theta = 63.75$ milliradians. The maximum range interval spanned by the central footprint is

$$R_{span} = R_{mx} - R_{mn} \quad (12.54)$$

$$R_{mx} = h / \cos(\beta^* + \theta/2) \quad (12.55)$$

$$R_{mn} = h / \cos(\beta^* - \theta/2) \quad (12.56)$$

Substituting the proper values from Table 12.1 into Eqs. (12.54), (12.55), and (12.56) yields

$$\{R_{span}, R_{mx}, R_{mn}\} = \{81.448, 1315.538, 1234.090\}m \quad (12.57)$$

which indicates that the system should have a total of 82 range bins. Doppler shift over the footprint is proportional to the radial velocity. It is given by

$$\frac{2v}{\lambda} \cos(90 + \theta/2) \sin\beta^* < f < \frac{2v}{\lambda} \cos(90 - \theta/2) \sin\beta^* \quad (12.58)$$

For this example, f_d is

TABLE 12.1. List of selected system parameters.

| Parameter | Symbol | Value |
|-----------------------------|-----------|-------------|
| <i># subintervals</i> | M | 64 |
| <i>size of array</i> | N | 32 |
| <i>wavelength</i> | λ | 3.19mm |
| <i>element spacing</i> | d | 16λ |
| <i>velocity</i> | v | 65m/s |
| <i>height</i> | h | 900m |
| <i>elevation angle</i> | β^* | 35° |
| <i>range resolution</i> | d_r | 1m |
| <i>observation interval</i> | D_{ob} | 20ms |

$$-1489.88\text{Hz} < f_d < 1489.88\text{Hz} \quad (12.59)$$

To avoid range and Doppler ambiguities the Pulse Repetition Frequency (PRF) should be

$$\frac{2v}{\lambda}\theta \leq PRF \leq \frac{c}{2R_{span}} \quad (12.60)$$

Using the system parameters defined in [Table 12.1](#), we find $5.995\text{KHz} \leq PRF \leq 1.31579\text{MHz}$. The DFT frequency resolution Δf is computed as the inverse of the observation interval, and it is equal to 50Hz . The size of the DFT, denoted as $NFFT$, is equal to the number of positions the antenna takes on along the flight path. The maximum Doppler variation resolved by this DFT is less than or equal to $\Delta f \times NFFT / 2$.

12.11. Arrays in Sequential Mode Operation

Standard Synthetic Aperture Radar (SAR) imaging systems are generally used to generate high resolution two-dimensional (2-D) images of ground terrain. Range gating determines resolution along the first dimension. Pulse compression techniques are usually used to achieve fine range resolution. Such techniques require the use of wide band receiver and display devices in order to resolve the time structure in the returned signals. The width of azimuth cells

provides resolution along the other dimension. Azimuth resolution is limited by the duration of the observation interval.

An approach for multiple target detection using linear arrays operated in sequential mode was previously presented by Mahafza. This technique is based on Discrete Fourier Transform (DFT) processing of equiphase data collected in sequential mode (DFTSQM). DFTSQM processing was also developed for 2-D real and synthetic arrays to include applications such as SAR imaging. The Field of View (FOV) of an array utilizing DFTSQM operation and signal processing is defined by the 3 dB beamwidth of a single element. Advantages of DFTSQM are (1) simultaneous detection of targets within the array's FOV without using any phase shifting hardware; and (2) the two-way array pattern is improved due to the coherent integration of equiphase returns. More specifically, the main lobe resolution is doubled while achieving a 27 dB sidelobe attenuation. However, the time required for transmission and processing may become a limitation when using this technique. A brief description of DFTSQM is presented in the next section.

12.11.1. Linear Arrays

Consider a linear array of size N , uniform element spacing d , and wavelength λ . Assume a far field scatterer P located at direction-sine $\sin\beta_l$. DFTSQM operation for this array can be described as follows. The elements are fired sequentially, one at a time, while all elements receive in parallel. The echoes are collected and integrated coherently on the basis of equal phase to compute a complex information sequence $\{b(m); m = 0, 2N - 1\}$. The x -coordinates, in d -units, of the x_n^{th} element with respect to the center of the array are

$$x_n = \left(-\frac{N-1}{2} + n\right); \quad n = 0, N-1. \quad (12.61)$$

The electric field received by the x_2^{th} element due to the firing of the x_1^{th} , and reflection by the l^{th} far field scatterer P is

$$E(x_1, x_2; s_l) = G^2(s_l) \left(\frac{R_0}{R}\right)^4 \sqrt{\sigma_l} \exp(j\phi(x_1, x_2; s_l)) \quad (12.62)$$

$$\phi(x_1, x_2; s_l) = \frac{2\pi}{\lambda}(x_1 + x_2)(s_l) \quad (12.63)$$

$$s_l = \sin\beta_l \quad (12.64)$$

where $\sqrt{\sigma_l}$ is the target cross section, $G^2(s_l)$ is the two-way element gain, and $(R_0/R)^4$ is the range attenuation with respect to reference range R_0 . The scatterer phase is assumed to be zero, however it could be easily included.

Assuming multiple scatterers in the array's FOV, the cumulative electric field in the path $x_1 \Rightarrow x_2$ due to reflection from all scatterers is

$$E(x_1, x_2) = \sum_{\text{all } l} [E_I(x_1, x_2; s_l) + jE_Q(x_1, x_2; s_l)] \quad (12.65)$$

where the subscripts (I, Q) denote the quadrature components. Note that the variable part of the phase given in Eq. (12.63) is proportional to the integers resulting from the sums $\{(x_{n1} + x_{n2}); (n1, n2) = 0, N-1\}$. In the far field operation there are a total of $(2N-1)$ distinct $(x_{n1} + x_{n2})$ sums. Therefore, the electric fields with paths of the same $(x_{n1} + x_{n2})$ sums can be collected coherently. In this manner the information sequence $\{b(m); m = 0, 2N-1\}$ is computed, where $b(2N-1)$ is set to equal zero. At the same time one forms the sequence $\{c(m); m = 0, 2N-2\}$ which keeps track of the number of returns that have the same $(x_{n1} + x_{n2})$ sum. More precisely, for $m = n1 + n2; (n1, n2) = 0, N-1$

$$b(m) = b(m) + E(x_{n1}, x_{n2}) \quad (12.66)$$

$$c(m) = c(m) + 1 \quad (12.67)$$

It follows that

$$\{c(m); m = 0, 2N-2\} = \left\{ \begin{array}{ll} m+1 & ; m = 0, N-2 \\ N & ; m = N-1 \\ 2N-1-m & m = N, 2N-2 \end{array} \right\} \quad (12.68)$$

which is a triangular shape sequence.

The processing of the sequence $\{b(m)\}$ is performed as follows: (1) the weighting takes the sequence $\{c(m)\}$ into account; (2) the complex sequence $\{b(m)\}$ is extended to size N_F , a power integer of two, by zero padding; (3) the DFT of the extended sequence $\{b'(m); m = 0, N_F-1\}$ is computed,

$$B(q) = \sum_{m=0}^{N_F-1} b'(m) \cdot \exp\left(-j\frac{2\pi qm}{N_F}\right); \quad q = 0, N_F-1 \quad (12.69)$$

and (4) after compensation for antenna gain and range attenuation, scatterers are detected as peaks in the amplitude spectrum $|B(q)|$. Note that step (4) is true only when

$$\sin\beta_q = \frac{\lambda q}{2Nd} \quad ; \quad q = 0, 2N-1 \quad (12.70)$$

where $\sin\beta_q$ denotes the direction-sine of the q^{th} scatterer, and $N_F = 2N$ is implied in Eq. (12.70).

The classical approach to multiple target detection is to use a phased array antenna with phase shifting and tapering hardware. The array beamwidth is proportional to (λ/Nd) , and the first sidelobe is at about -13 dB. On the other hand, multiple target detection using DFTSQM provides a beamwidth proportional to $(\lambda/2Nd)$ as indicated by Eq. (12.70), which has the effect of doubling the array's resolution. The first sidelobe is at about -27 dB due the triangular sequence $\{c(m)\}$. Additionally, no phase shifting hardware is required for detection of targets within a single element field of view.

12.11.2. Rectangular Arrays

DFTSQM operation and signal processing for 2-D arrays can be described as follows. Consider an $N_x \times N_y$ rectangular array. All $N_x N_y$ elements are fired sequentially, one at a time; after each firing, all the $N_x N_y$ array elements receive in parallel. Thus, $N_x N_y$ samples of the quadrature components are collected after each firing, and a total of $(N_x N_y)^2$ samples will be collected. However, in the far field operation, there are only $(2N_x - 1) \times (2N_y - 1)$ distinct equiphase returns. Therefore, the collected data can be added coherently to form a 2-D information array of size $(2N_x - 1) \times (2N_y - 1)$. The two-way radiation pattern is computed as the modulus of the 2-D amplitude spectrum of the information array. The processing includes 2-D windowing, 2-D Discrete Fourier Transformation, antenna gain, and range attenuation compensation. The field of view of the 2-D array is determined by the 3 dB pattern of a single element. All the scatterers within this field will be detected simultaneously as peaks in the amplitude spectrum.

Consider a rectangular array of size $N \times N$, with uniform element spacing $d_x = d_y = d$, and wavelength λ . The coordinates of the n^{th} element, in d -units, are

$$x_n = \left(-\frac{N-1}{2} + n \right) \quad ; \quad n = 0, N-1 \quad (12.71)$$

$$y_n = \left(-\frac{N-1}{2} + n \right) \quad ; \quad n = 0, N-1 \quad (12.72)$$

Assume a far field point P defined by the azimuth and elevation angles (α, β) . In this case, the one-way geometric phase for an element is

$$\varphi'(x, y) = \frac{2\pi}{\lambda} [x \sin \beta \cos \alpha + y \sin \beta \sin \alpha] \quad (12.73)$$

Therefore, the two-way geometric phase between the (x_1, y_1) and (x_2, y_2) elements is

$$\varphi(x_1, y_1, x_2, y_2) = \frac{2\pi}{\lambda} \sin \beta [(x_1 + x_2) \cos \alpha + (y_1 + y_2) \sin \alpha] \quad (12.74)$$

The two-way electric field for the l^{th} scatterer at (α_l, β_l) is

$$E(x_1, x_2, y_1, y_2; \alpha_l, \beta_l) = G^2(\beta_l) \left(\frac{R_0}{R}\right)^4 \sqrt{\sigma_l} \exp[j(\varphi(x_1, y_1, x_2, y_2))] \quad (12.75)$$

Assuming multiple scatterers within the array's FOV, then the cumulative electric field for the two-way path $(x_1, y_1) \Rightarrow (x_2, y_2)$ is given by

$$E(x_1, x_2, y_1, y_2) = \sum_{\text{all scatterers}} E(x_1, x_2, y_1, y_2; \alpha_l, \beta_l) \quad (12.76)$$

All formulas for the 2-D case reduce to those of a linear array case by setting $N_y = 1$ and $\alpha = 0$.

The variable part of the phase given in Eq. (12.74) is proportional to the integers $(x_1 + x_2)$ and (y_1, y_2) . Therefore, after completion of the sequential firing, electric fields with paths of the same (i, j) sums, where

$$\{i = x_{n1} + x_{n2}; i = -(N-1), (N-1)\} \quad (12.77)$$

$$\{j = y_{n1} + y_{n2}; j = -(N-1), (N-1)\} \quad (12.78)$$

can be collected coherently. In this manner the 2-D information array $\{b(m_x, m_y); (m_x, m_y) = 0, 2N-1\}$ is computed. The coefficient sequence $\{c(m_x, m_y); (m_x, m_y) = 0, 2N-2\}$ is also computed. More precisely,

$$\text{for } m_x = n1 + n2 \text{ and } m_y = n1 + n2; \quad (12.79) \\ n1 = 0, N-1, \text{ and } n2 = 0, N-1$$

$$b(m_x, m_y) = b(m_x, m_y) + E(x_{n1}, y_{n1}, x_{n2}, y_{n2}) \quad (12.80)$$

It follows that

$$c(m_x, m_y) = (N_x - |m_x - (N_x - 1)|) \times (N_y - |m_y - (N_y - 1)|) \quad (12.81)$$

The processing of the complex 2-D information array $\{b(m_x, m_y)\}$ is similar to that of the linear case with the exception that one should use a 2-D DFT. After antenna gain and range attenuation compensation, scatterers are detected as peaks in the 2-D amplitude spectrum of the information array. A scatterer located at angles (α_l, β_l) will produce a peak in the amplitude spectrum at DFT indexes (p_l, q_l) , where

$$\alpha_l = \text{atan}\left(\frac{q_l}{p_l}\right) \quad (12.82)$$

$$\sin\beta_l = \frac{\lambda p_l}{2Nd\cos\alpha_l} = \frac{\lambda q_l}{2Nd\sin\alpha_l} \quad (12.83)$$

In order to prove Eq. (12.82), consider a rectangular array of size $N \times N$, with uniform element spacing $d_x = d_y = d$, and wavelength λ . Assume sequential mode operation where elements are fired sequentially, one at a time, while all elements receive in parallel. Assuming far field observation defined by azimuth and elevation angles (α, β) . The unit vector \vec{u} on the line of sight, with respect to \vec{O} , is given by

$$\vec{u} = \sin\beta\cos\alpha\vec{a}_x + \sin\beta\sin\alpha\vec{a}_y + \cos\beta\vec{a}_z \quad (12.84)$$

The $(n_x, n_y)^{th}$ element of the array can be defined by the vector

$$\vec{e}(n_x, n_y) = \left(n_x - \frac{N-1}{2}\right)d\vec{a}_x + \left(n_y - \frac{N-1}{2}\right)d\vec{a}_y \quad (12.85)$$

where $(n_x, n_y = 0, N-1)$. The one-way geometric phase for this element is

$$\varphi'(n_x, n_y) = k(\vec{u} \bullet \vec{e}(n_x, n_y)) \quad (12.86)$$

where $k = 2\pi/\lambda$ is the wave-number, and the operator (\bullet) indicates dot product. Therefore, the two-way geometric phase between the (n_{x1}, n_{y1}) and (n_{x2}, n_{y2}) elements is

$$\varphi(n_{x1}, n_{y1}, n_{x2}, n_{y2}) = k[\vec{u} \bullet \{\vec{e}(n_{x1}, n_{y1}) + \vec{e}(n_{x2}, n_{y2})\}] \quad (12.87)$$

The cumulative two-way normalized electric due to all transmissions in the direction (α, β) is

$$E(\vec{u}) = E_t(\vec{u})E_r(\vec{u}) \quad (12.88)$$

where the subscripts t and r , respectively, refer to the transmitted and received electric fields. More precisely,

$$E_t(\vec{u}) = \sum_{n_{xt}=0}^{N-1} \sum_{n_{yt}=0}^{N-1} w(n_{xt}, n_{yt}) \exp[jk\{\vec{u} \bullet \vec{e}(n_{xt}, n_{yt})\}] \quad (12.89)$$

$$E_r(\vec{u}) = \sum_{n_{xr}=0}^{N-1} \sum_{n_{yr}=0}^{N-1} w(n_{xr}, n_{yr}) \exp[jk\{\vec{u} \bullet \vec{e}(n_{xr}, n_{yr})\}] \quad (12.90)$$

In this case, $w(n_x, n_y)$ denotes the tapering sequence. Substituting Eqs. (12.87), (12.89), and (12.90) into Eq. (12.88) and grouping all fields with the same two-way geometric phase yield

$$E(\vec{u}) = e^{j\delta} \sum_{m=0}^{N_a-1} \sum_{n=0}^{N_a-1} w'(m, n) \exp[jkd \sin \beta (m \cos \alpha + n \sin \alpha)] \quad (12.91)$$

$$N_a = 2N - 1 \quad (12.92)$$

$$m = n_{xt} + n_{xr}; m = 0, 2N - 2 \quad (12.93)$$

$$n = n_{yt} + n_{yr}; n = 0, 2N - 2 \quad (12.94)$$

$$\delta = \left(\frac{-d \sin \beta}{2} \right) (N - 1) (\cos \alpha + \sin \alpha) \quad (12.95)$$

The two-way array pattern is then computed as

$$|E(\vec{u})| = \left| \sum_{m=0}^{N_a-1} \sum_{n=0}^{N_a-1} w'(m, n) \exp[jkd \sin \beta (m \cos \alpha + n \sin \alpha)] \right| \quad (12.96)$$

Consider the two-dimensional DFT transform, $W'(p, q)$, of the array $w'(n_x, n_y)$

$$W'(p, q) = \sum_{m=0}^{N_a-1} \sum_{n=0}^{N_a-1} w'(m, n) e^{-j \frac{2\pi}{N_a} (pm + qn)} ; (p, q) = 0, N_a - 1 \quad (12.97)$$

Comparison of Eq. (12.96) and (12.97) indicates that $|E(\vec{u})|$ is equal to $|W(p, q)|$ if

$$-\left(\frac{2\pi}{N_a}\right)p = \frac{2\pi}{\lambda}d\sin\beta\cos\alpha \quad (12.98)$$

$$-\left(\frac{2\pi}{N_a}\right)q = \frac{2\pi}{\lambda}d\sin\beta\sin\alpha \quad (12.99)$$

It follows that

$$\alpha = \tan^{-1}\left(\frac{q}{p}\right) \quad (12.100)$$

which is the same as Eq. (12.82).

12.12. MATLAB Programs

This section contains the MATLAB programs used in this chapter.

Listing 12.1. MATLAB Program “fig12_2.m”

```
clear all
var = -pi:0.001:pi;
y1 = (sinc(var)).^2;
y2 = abs(sinc(2.0 * var));
plot (var,y1,var,y2);
axis tight
grid;
xlabel ('angle - radians');
ylabel ('array pattern');
```

Problems

12.1. A side looking SAR is traveling at an altitude of 15 Km ; the elevation angle is $\beta = 15^\circ$. If the aperture length is $L = 5\text{ m}$, the pulse width is $\tau = 20\mu\text{ s}$ and the wavelength is $\lambda = 3.5\text{ cm}$. (a) Calculate the azimuth resolution. (b) Calculate the range and ground range resolutions.

12.2. A MMW side looking SAR has the following specifications: radar velocity $v = 70\text{ m/s}$, elevation angle $\beta = 35^\circ$, operating frequency $f_0 = 94\text{ GHz}$, and antenna 3dB beam width $\theta_{3dB} = 65\text{ mrad}$. (a) Calculate

the footprint dimensions. (b) Compute the minimum and maximum ranges. (c) Compute the Doppler frequency span across the footprint. (d) Calculate the minimum and maximum PRFs.

12.3. A side looking SAR takes on eight positions within an observation interval. In each position the radar transmits and receives one pulse. Let the distance between any two consecutive antenna positions be d , and define

$\delta = 2\pi\frac{d}{\lambda}(\sin\beta - \sin\beta_0)$ to be the one-way phase difference for a beam steered

at angle β_0 . (a) In each of the eight positions a sample of the phase pattern is obtained after heterodyning. List the phase samples. (b) How will you process the sequence of samples using an FFT (do not forget windowing)? (c) Give a formula for the angle between the grating lobes.

12.4. Consider a synthetic aperture radar. You are given the following Doppler history for a scatterer: $\{1000Hz, 0, -1000HZ\}$ which corresponds to times $\{-10ms, 0, 10ms\}$. Assume that the observation interval is $T_{ob} = 20ms$, and a platform velocity $v = 200m/s$. (a) Show the Doppler history for another scatterer which is identical to the first one except that it is located in azimuth $1m$ earlier. (b) How will you perform deramping on the quadrature components (show only the general approach)? (c) Show the Doppler history for both scatterers after deramping.

12.5. You want to design a side looking synthetic aperture Ultrasonic radar operating at $f_0 = 60KHz$ and peak power $P_t = 2W$. The antenna beam is conical with 3dB beam width $\theta_{3dB} = 5^\circ$. The maximum gain is 16. The radar is at a constant altitude $h = 15m$ and is moving at a velocity of $10m/s$. The elevation angle defining the footprint is $\beta = 45^\circ$. (a) Give an expression for the antenna gain assuming a Gaussian pattern. (b) Compute the pulse width corresponding to range resolution of $10mm$. (c) What are the footprint dimensions? (d) Compute and plot the Doppler history for a scatterer located on the central range bin. (e) Calculate the minimum and maximum PRFs; do you need to use more than one PRF? (f) How will you design the system in order to achieve an azimuth resolution of $10mm$?

12.6. Derive Eq. (12.45) through Eq. (12.47).

12.7. In Section 12.7 we assumed the elevation angle increment ϵ is equal to zero. Develop an equivalent to Eq. (12.43) for the case when $\epsilon \neq 0$. You need to use a third order three-dimensional Taylor series expansion about the state $(t, \mu, \epsilon) = (0, 0, 0)$ in order to compute the new round-trip delay expression.